Ceramics International 45 (2019) 11989–12000

Contents lists available at ScienceDirect

Ceramics International

journal homepage: www.elsevier.com/locate/ceramint

Frequency and dc bias voltage dependent dielectric properties and electrical conductivity of $BaTiO_3$–$SrTiO_3/(SiO_2)_x$ nanocomposites

Y. Slimani[a,*], B. Unal[b], E. Hannachi[c,**], A. Selmi[d,e], M.A. Almessiere[a,f], M. Nawaz[g], A. Baykal[g], I. Ercan[a], M. Yildiz[h]

[a] Department of Physics Research, Institute for Research & Medical Consultations (IRMC), Imam Abdulrahman Bin Faisal University, P.O. Box 1982, Dammam, 31441, Saudi Arabia
[b] Department of Software and Computer Engineering, Istanbul Sabahattin Zaim University, Halkali Cad. No: 2, 34303, Halkali-Kucukcekmece, Istanbul, Turkey
[c] Laboratory of Physics of Materials - Structures and Properties, Department of Physics, Faculty of Sciences of Bizerte, University of Carthage, Zarzouna, 7021, Tunisia
[d] Laboratoire Matériaux Organisation et Propriétés (LMOP), Université de Tunis El Manar, Campus Universitaire, 2092, El Manar, Tunis/Tunisie
[e] Unité de Dynamique et Structure des Matériaux Moléculaires, Université du Littoral Côte d'Opale, 50 rue Ferdinand Buisson, 62228, Calais Cedex, France
[f] Department of Physics, College of Science, Imam Abdulrahman Bin Faisal University, P.O. Box 1982, 31441, Dammam, Saudi Arabia
[g] Department of Nano-Medicine Research, Institute for Research & Medical Consultations (IRMC), Imam Abdulrahman Bin Faisal University, P.O. Box 1982, 31441, Dammam, Saudi Arabia
[h] Corrosion Research Laboratory, Department of Mechanical Engineering, Faculty of Engineering, Duzce University, 81620, Duzce, Turkey

ARTICLE INFO

Keywords:
$BaTiO_3$-$SrTiO_3$
SiO_2
Structure
Morphology
Dielectric properties

ABSTRACT

$BaTiO_3$–$SrTiO_3/(SiO_2)_x$ nanocomposites (x = 0, 0.5, 1, 2 and 5%) were produced through solid state reaction. The morphological, structural, spectral, and optical properties were investigated by scanning electron microscope, X-ray powder diffraction (XRD), Fourier transform-infrared spectroscopy and ultraviolet–visible diffuse reflectance spectrophotometry, respectively. All XRD patterns illustrate two distinct phases of $BaTiO_3$ and $SrTiO_3$ with cubic structure. No impurity was noticed for $x \leq 0.5\%$ nanocomposite. However, $Ba_2TiSi_2O_8$ secondary phase starts to appear for $x \geq 1\%$. Electrical and dielectric properties were used to analyze the dielectric constant and loss, the conductivity as well as dissipation factors as functions of both frequencies and dc bias voltage for $BaTiO_3$–$SrTiO_3/(SiO_2)_x$ nanocomposites. In general, conductivity and dielectric loss obey power law tendencies against frequencies. However, the dc bias was found to be less effective to conduction mechanism having a slight change for a variety of SiO_2 percentages.

1. Introduction

The investigation on ferroelectric metal oxide with the perovskite structure ABO_3 has received considerable scientific interest owing to their excellent ferroelectric, dielectric, photoelectric, piezoelectric, pyroelectric, and catalytic responses [1–3]. The family of perovskites involves many titanate-based materials that are utilized in numerous technological applications such as electronics, electro-mechanical and electro-optical applications.

Barium titanate $BaTiO_3$ (noted BTO hereafter) is a familiar ferroelectric material exhibiting an important resistivity and dielectric constant. These features make BTO a promising candidate for various applications. BTO is largely used to produce electronic devices for example multilayer capacitors, passive memory storage devices, nonlinear resistors, positive temperature coefficient thermistors, thermal switches, piezoelectric transducers and actuators, gas sensors and many electro-optical devices [4,5]. The major concentration in BTO comes from its ferroelectric properties at room temperature in which the Curie temperature is about 120 °C [6]. Another well-known piezoelectric and ferroelectric compound is the $SrTiO_3$ (noted STO hereafter) which has a cubic structure. STO is frequently utilized in similar applications like BTO but at much lower temperatures [7]. Moreover, the STO exhibit band gap of 3.2 eV, superior photo-chemical and chemical stability, high catalytic activity and better biological compatibility that make it promising in various practical applications [8].

Nowadays, barium strontium titanate mixture has being a great interest electronic material because of its lower dielectric loss, greater dielectric constant, adjustable Curie temperature and higher tunability of dielectric performances compared to BTO and STO alone [9–13]. The barium strontium titanate (noted BT-ST hereafter) materials display

* Corresponding author.
** Corresponding author.
E-mail addresses: yaslimani@iau.edu.sa, slimaniyassine18@gmail.com (Y. Slimani), hannechi.essia@gmail.com (E. Hannachi).

https://doi.org/10.1016/j.ceramint.2019.03.092
Received 21 February 2019; Received in revised form 2 March 2019; Accepted 13 March 2019
Available online 16 March 2019

promising ferroelectric, piezoelectric and pyroelectric characteristics leading them to be extensively utilized in the manufacture of uncooled infrared detectors, piezoelectric sensors, high dielectric capacitors, dynamic random-access memories, microwave phase shifters, transducers and PTC resistors [9–13]. Two phases, one ferroelectric tetragonal and the other paraelectric cubic, coexist at the BT-ST composition at ambient temperature. Numerous approaches are used to synthesize nanosized BT-ST material, such as solid-state reaction method through high-temperature synthesis in solids or mechanochemical synthesis [14], sol–gel process [15], hydrothermal method [16], chemical co-precipitation [17], etc. The high-energy ball milling lead to obtain titanium-based perovskites having better dielectric properties compared to those prepared through high-temperature synthesis [18,19].

Due to demands of peoples, the dielectric properties of ceramics materials are increasing amazingly. However, in the diverse above-mentioned technological applications, the control of the microstructure is required to enhance their performances. The microstructure depends on specific treating parameters including temperature and occurrence of impurities or dopants. Various kinds of additives have been used and greatly affected the dielectric properties of perovskites ceramics [20–23]. Recently, composites of ferroelectric ceramics and glasses have attracted a special attention in technological applications like energy storage materials. Oxide glasses were extensively employed as glass constituents in the ceramic-glass composites because of their low dielectric loss and high breakdown strength [24,25]. A variety of glass materials have been added to BTO and STO ceramics. Among them, SiO_2 is an economic and effective additive to enhance the properties of ferroelectric ceramics. Numerous studies have been done on BTO-SiO_2 [26–30] and STO-SiO_2 composites [31,32]. Such content of SiO_2 added to BTO or STO ceramics showed an improvement in dielectric properties. For example, Yanjie Luo et al. [26] synthesized $BaTiO_3$—SiO_2 ceramics by microwave sintering method. The authors showed that SiO_2 has a great influence on the dielectric properties of BTO ceramics. The permittivity reached the maximum value and the dielectric loss had the minimum value when the SiO_2 content is 0.4 mol%. M. Cernea et al. [29] prepared core–shell structured of (BT-$Nb_{0.005}$)/SiO_2 particles via sol–gel technique. It was found that (BT-$Nb_{0.005}$)/SiO_2 core–shell composite exhibits smaller dielectric constant and smaller dissipation factor compared to uncoated BT-$Nb_{0.005}$. The synthsized (BT-$Nb_{0.005}$)/SiO_2 core–shell material is considered to be promising for application in the composite heterostructure capacitors.

The SiO_2 was added into STO by Chun-Chieh Lin et al. [32]. Their findings show that the prepared STO-SiO_2 films exhibited good electrical properties, making them good candidates for alternative high-*k* gate dielectric applications.

To the best of our acknowledge, the use of SiO_2 as a doping in the BT-ST ceramics has not been yet studied in the literature. In this study, we investigate deeply the structural, microstructural, spectral, optical and dielectric properties of BT-ST/$(SiO_2)_x$ nanocomposites, where x = 0, 0.5, 1, 2 and 5%.

2. Experimental

Commercial high purity (99.99%) nanopowders of $BaTiO_3$—$SrTiO_3$ (noted BT-ST hereafter) with a particle size < 100 nm and SiO_2 with an average particles size of 15 nm were selected as raw materials and purchased from Sigma Aldrich company. The raw nanopowders were mixed stoichiometrically in accordance to the designed compositions BT-ST/$(SiO_2)_x$ where x = 0%, 0.5%, 1%, 2% and 5%. Then, the mixtures were sintered at 1100 °C for 4 h. The obtained nanocomposites were grinded by planetary high energy ball milling (HEBM) as a grinding media in ethanol for 12 h. After drying, the grinded nanocomposites were compacted into discs having a diameter of 13 mm and sintered at 1100 °C for 4 h in air atmosphere.

The phase identification was examined by X-ray powder diffraction (XRD; Rigaku Benchtop Miniflex) using Cu-kα radiation. The morphology was investigated by scanning electron microscope (SEM; FEI Quanta FEG). Fourier transform-infrared (FT-IR) spectra were collected using Bruker alpha-II FT-IR spectrometer in wavenumbers of 4000–400 cm^{-1}. The diffuse reflectance spectra (DRS) were registered using UV–Vis spectrophotometer (JASCO V-780). The electrical and dielectric measurements were done by using Novocontrol Technologies (Alpha-N high-resolution analyzer).

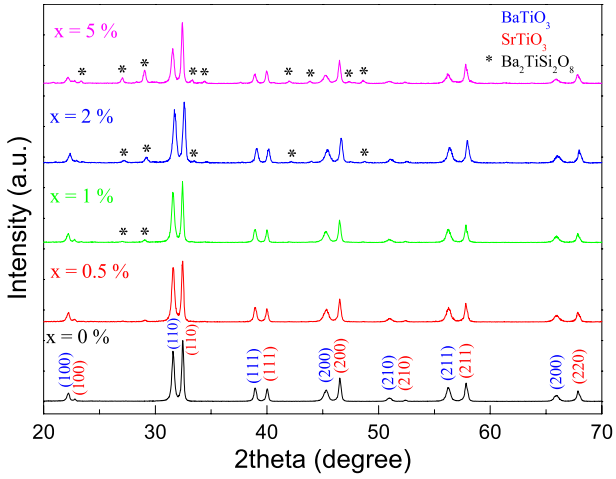

Fig. 1. XRD patterns of various synthesized BT-ST/$(SiO_2)_x$ nanocomposites.

3. Results and discussion

3.1. Structural examination

XRD patterns of various synthesized BT-ST/$(SiO_2)_x$ nanocomposites (x = 0%, 0.5%, 1%, 2%, and 5%) are presented in Fig. 1. The phase fractions and lattice parameters are determined through Rietveld refinement by using Match program and are listed in Table 1. All XRD patterns illustrate two distinct phases of BTO (ICCD No. 96-150-7758) with larger lattice parameter and STO (ICCD No. 96-721-2246) with smaller lattice constant. The two phases crystallize in cubic structure with *Pm3m* group space. No such impurity was noticed in pure BT-ST sample (i.e. x = 0%) and x = 0.5% nanocomposite. However, some impurity peaks (marked as '*') related to the $Ba_2TiSi_2O_8$ phase (ICCD No. 96-153-0354) starts to appear with further increasing SiO_2 doping (i.e. x ≥ 1%). The concentration of this secondary phase increases gradually with increasing the SiO_2 doping content.

3.2. Morphological investigation

SEM micrographs of the selected BT-ST/$(SiO_2)_x$ nanocomposites with x = 0%, 1%, 2% and 5% are showed in Fig. 2. Pure BT-ST sample (Fig. 2(a)) illustrated a morphology with homogeneous nanosized grains. No noticeable variation in the microstructure was observed with SiO_2. Elemental mapping analyses were performed for the two selected

Table 1
Phase fractions and lattice parameters of different prepared BT-ST/$(SiO_2)_x$ nanocomposites.

x % of SiO_2	*Phase fractions (%)*			*Lattice parameters*	
	BTO	*STO*	*Impurity*	a_{BTO} *(Å)*	a_{STO} *(Å)*
0	53.1	46.9	0.0	4.0083	3.9058
0.5	52.9	47.1	0.0	4.0057	3.9059
1	49.0	47.4	3.6	4.0070	3.9057
2	44.9	48.0	7.2	4.0075	3.9057
5	33.8	49.3	16.9	4.0079	3.9056

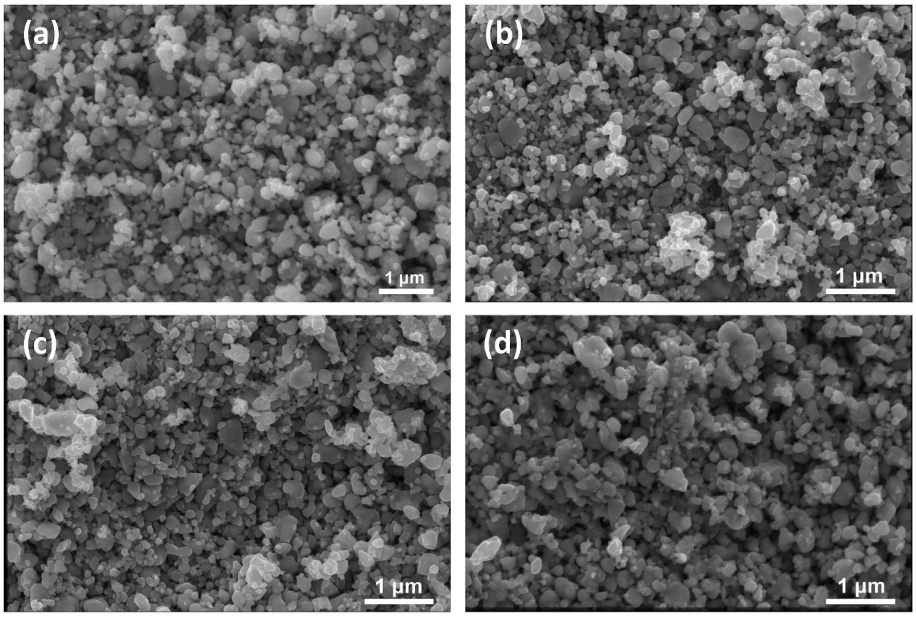

Fig. 2. SEM micrographs of synthesized BT-ST/$(SiO_2)_x$ nanocomposites where x = 0, 1, 2 and 5%.

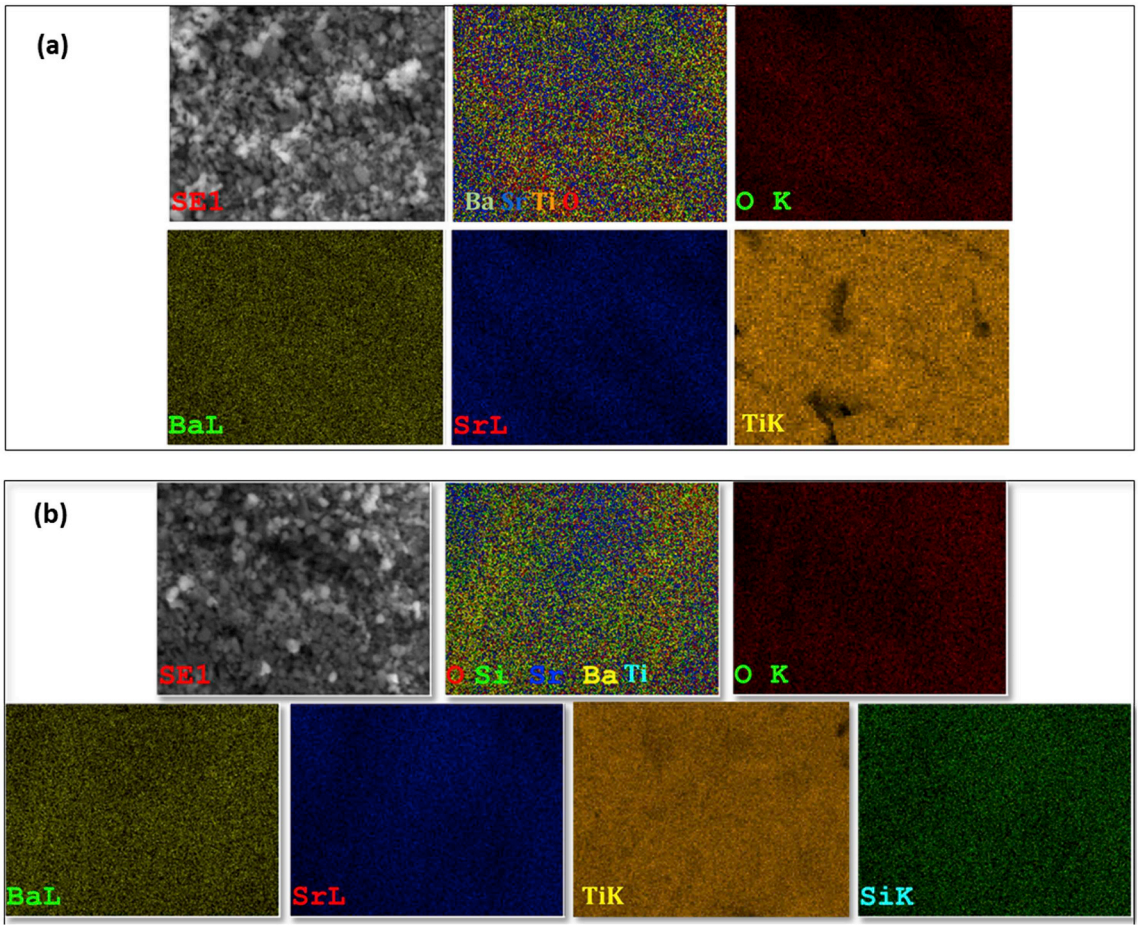

Fig. 3. Elemental mapping for the two selected **(a)** x = 0% and **(b)** x = 2% nanocomposites.

x = 0% and 2% samples and presented in Fig. 3. The analysis of x = 0% sample confirmed the existence of the elements of barium (Ba), strontium (Sr), titanium (Ti), and oxygen (O). The analysis of x = 2% showed the presence of silicium (Si) in addition to Ba, Sr, Ti and O elements.

3.3. FT-IR analysis

Fig. 4 illustrates the FT-IR spectra of BT-ST/$(SiO_2)_x$ nanocomposites (x = 0%, 0.5%, 1%, 2%, and 5%). The absorption band at 545 cm^{-1} is corresponding to the metal-oxygen stretching vibrations of Ti—O bonds,

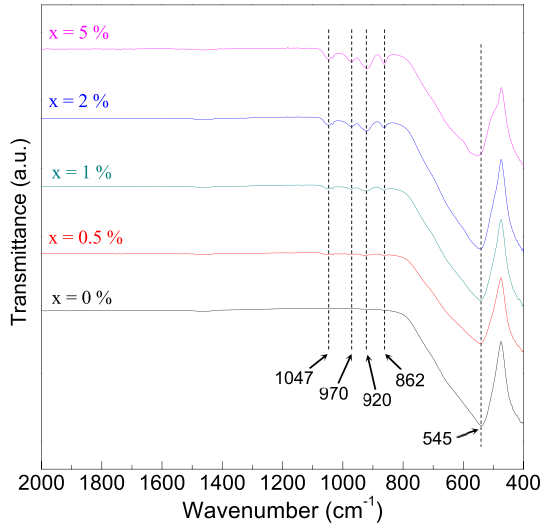

Fig. 4. FT-IR spectra of BT-ST/$(SiO_2)_x$ nanocomposites where x = 0, 0.5, 1, 2 and 5%.

which confirmed the formation of BT-ST [33,34]. It is well-known that the existence of absorption bands around 3440 and 1630 cm^{-1} are associated to the H—O—H stretching modes and the bending vibrations of the absorbed water, respectively [33,34]. Furthermore, it is reported that the peaks corresponding to carbonate groups appear around 1440 cm^{-1} [33,34]. In the present study, no such peak is found around 3440, 1630 and 1440 cm^{-1} for all samples, indicating that the molecules of water and carbon are disappeared owing to the calcination effect at high temperatures. This confirms the high purity of obtained nanocomposites. Compared to pure BT-ST one, new bonds are perceived in the range between 860 and 1050 cm^{-1} for BT-ST samples doped with SiO_2 ($x \geq 0.5\%$), which are assigned to the SiO_2 components [35,36]. The characteristic absorption bands at 970 and 1050 cm^{-1} are ascribed to the vibrations of Si—O—Si stretching bonds, while those at 920 and 860 cm^{-1} are assigned to the Si—O bending vibrations. It is obvious that the intensity of these peaks (between 860 and 1050 cm^{-1}) enhances with increasing x, showing that the silica content increases. The obtained FT-IR results verify the formation of the desired BT-ST/$(SiO_2)_x$ nanocomposites.

3.4. Optical analysis

Optical properties of BT-ST/$(SiO_2)_x$ nanocomposites were studied in the range 200–800 nm and obtained DRS spectra are shown in the Fig. 5. We used Kubelka-Munk approach to estimate the band gap energy (E_g) of BT-ST/$(SiO_2)_x$ nanocomposites [37]. Tauc plots ($(\alpha h\nu)^2$ *vs.* photon energy ($h\nu$)) lead to determine the E_g values of BT-ST/$(SiO_2)_x$ nanocomposites as shown in Fig. 6. The E_g values for x = 0%, 0.5%, 1%, 2% and 5% are equal to 3.22, 3.30, 3.30, 3.38, 3.33 eV, respectively. The obtained E_g values are higher for various BT-ST/(SiO_2) nanocomposites compared to the pristine one. The value of band gap is increased with increasing x content up to x = 2%. The increased in E_g value could be ascribed to the development of energy level or interface defects in BT-ST/$(SiO_2)_x$ nanocomposites [38]. For higher content of SiO_2 (x = 5%), the E_g value decreased. This reduction is possibly resulting from the formation of sub-bands in between the energy band gaps and merging of their sub-bands with the conduction bands to form a continuous band [39]. Other various factors such presence of impurities, lattice strain and crystallites size could be the reason of reduction of band gap [40].

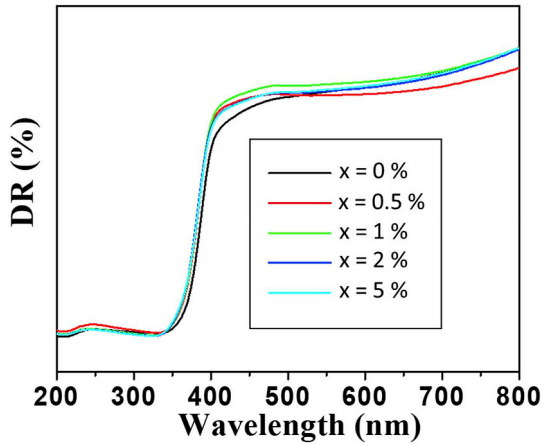

Fig. 5. Diffuse reflectance spectra of BT-ST/$(SiO_2)_x$ nanocomposites.

3.5. Analysis of impedance spectroscopy, electrical conductivity and dielectric properties

The investigation of complex impedance spectra is a powerful method employed effectively to evaluate the dielectric and electrical properties of many electroceramics including conductivity, dielectric behavior and relaxation properties. These analyzes make it possible to realize the contributions of various processes, for example grain size effect and interface properties, or functional grain-grain boundaries. This also contains a variety of properties such as conductivity, dielectrics, for the function of frequency, external electric field as well as level and distribution of various additives. Based on spectroscopic analysis, the impedance of sub-micron-sized grains could be isolated from that of grain boundaries, which is more apparent at low frequency as well as electrode effects [41]. Thus, an equivalent circuit on the basis of complex impedance spectra provides some perspectives on physical development in the BT-ST/$(SiO_2)_x$ nanocomposites. That is, the equivalent arrangement consists of a series of two sub-systems; one leads to grain effects, and the other to grain boundaries [42]. For the typical assessment of complex impedance spectra, the signal response to stimuli *ac* electric field is synchronized with an informative regulation of Fourier transformation. Therefore, it is emphasized that the complex dielectric mechanism is represented with the following expression as:

$$\varepsilon^*(\omega,\cdot x) = \varepsilon_r'(\omega,\cdot x) - i\varepsilon_r''(\omega,r)$$

So, the complex conductivity is given as:

$$\sigma^*(\omega,x) = \sigma'(\omega,x) - i\,\sigma''(\omega,x)$$

where $\omega = 2\pi f$ is the angular frequency.

The dielectric constant (ε_r') and dielectric loss (ε_r''), dielectric tangent loss ($tan\delta$) and *ac* conductivity (σ_{ac}) are deduced by the following standard expression;

$$\varepsilon'(\omega,x) = \frac{C(\omega,x)d}{\varepsilon_0 A}$$

where C stands for the measured capacitance, A is the cross-sectional overlapping area of pellet, d is the gap among two coupled electrodes, and ε_0 is dielectric permittivity of the vacuum. It is clear to note that *ac* conductivity is acquired from dielectric loss $\varepsilon''(\omega)$ as follows;

$$\sigma_{ac}(\omega,x) = \omega\varepsilon_0\varepsilon''(\omega,x) = \omega\varepsilon_0\varepsilon'(\omega,x)tan\delta$$

in relation to a tangent formulation of

$$\varepsilon''(\omega,x) = \varepsilon'(\omega' x)tan\delta$$

It is emphasized firmly that the frequency-dependent characterization for conduction mechanism is a convenient evaluation to evaluate transport progression in a variety of NPs additives. In most of compositional NPs, a comprehensive conductivity could be assigned into two parts; the *dc* conductivity owing to "*band conduction*" and the *ac* conductivity owing to "*hopping mechanism*" caused by transitional charge

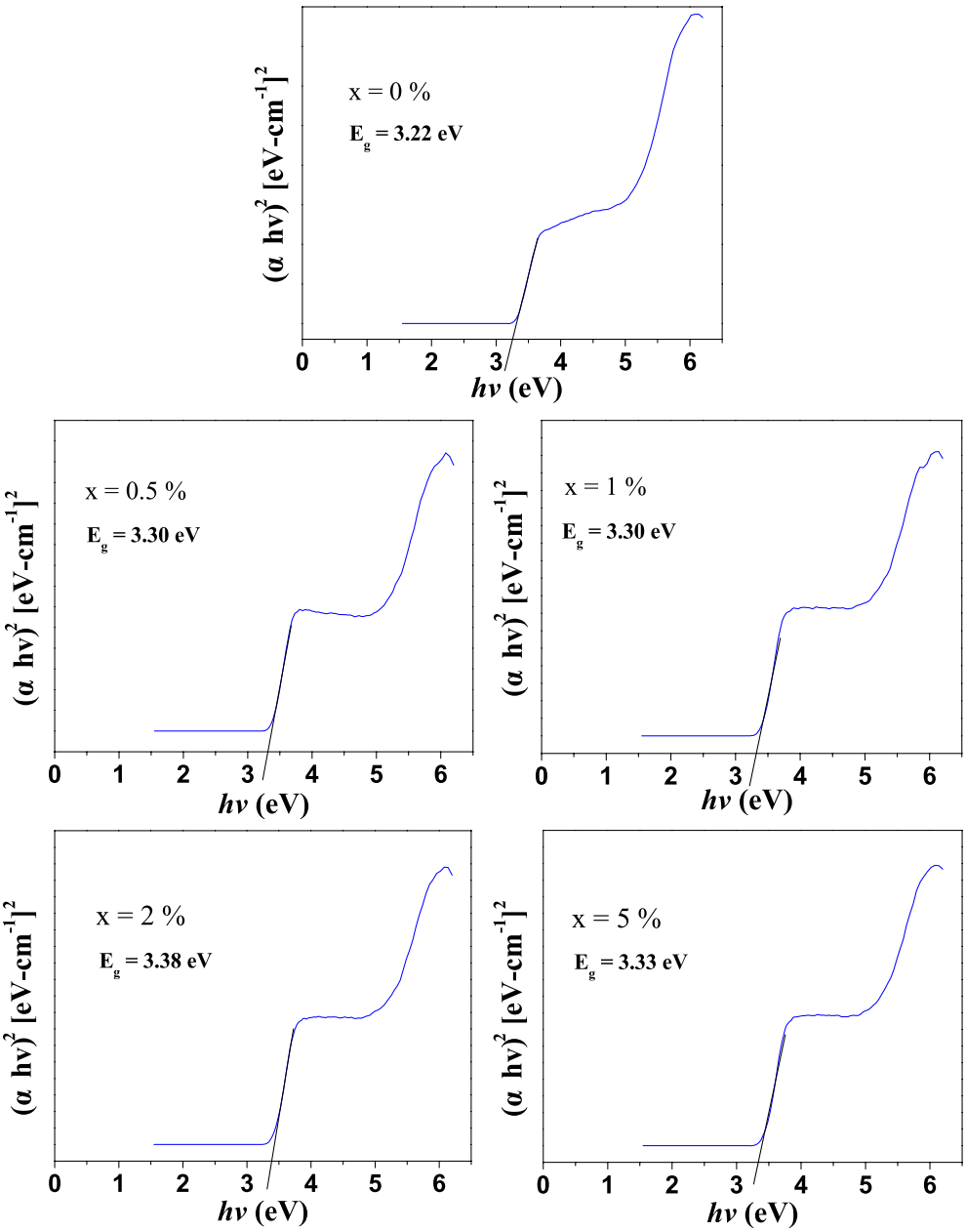

Fig. 6. Plots of $(\alpha h\upsilon)^2$ versus photon energy of prepared BT-ST/$(SiO_2)_x$ nanocomposites for estimating the band gap energy.

carriers among the same ions of a certain element emerging in several valence states. This can be attributable to a tendency of the power law dependency as explained in the next sections [43].

Considering the above theoretical interpretations, σ_{ac}, ε', ε'', $tan\delta$, and dissipation factor were examined as functions of SiO_2 content, frequency, and *dc* bias voltage. So, these parameters could be considered to be very important for the application of BT-ST ceramics or films in microelectronic devices [41,42].

3.5.1. Electrical conduction mechanism

The ac conductivity measurements at room temperature of BT-ST/$(SiO_2)_x$ nanocomposites were performed versus frequency in the bias range of −20 V – +20 V. The dependences of σ_{ac} on frequency up to 10 MHz and dc bias ranging from −20 V to 20 V presented in Fig. 7 were given by means of the following expression [44,45]:

$$\sigma'(\omega, x) = \sigma_{ac}(\omega, x) = \varepsilon_r''(\omega, x)\omega\varepsilon_0$$

It is also seen clearly from the graphs that all the conductivities illustrate almost linear variation in *log-log* plot while less influences are observed for dc bias application. This means that conductivity obeys a power law against frequency with a certain exponent value, *n* as follows:

$$\sigma(\omega, T, x) = \sigma(T, x)\omega^n$$

where '*n*' varies slightly with a SiO_2 weight percentages (%), but leads to a less dependency on the applied *dc* bias. Fig. 7 also shows that the conductivity at frequencies up to 100 kHz has less influence, but indicates that a sharp escalation is recorded over it for all SiO_2 contents. It can be clearly seen that tendencies are depicted a discernible variation in conductivity against the SiO_2 concentration. Here the x = 1% curve gives us a higher conductive tendency than the one in the x = 2% curve, while the x = 0.5% and 5% curves own a similar tendency for frequencies ranging up to 10 MHz. It is obvious to emphasize that two types of the attitude in conductivity variation are clearly seen at frequencies below and above 200 kHz. This can be the reason of the reactive effect leading over conductivity at higher frequencies.

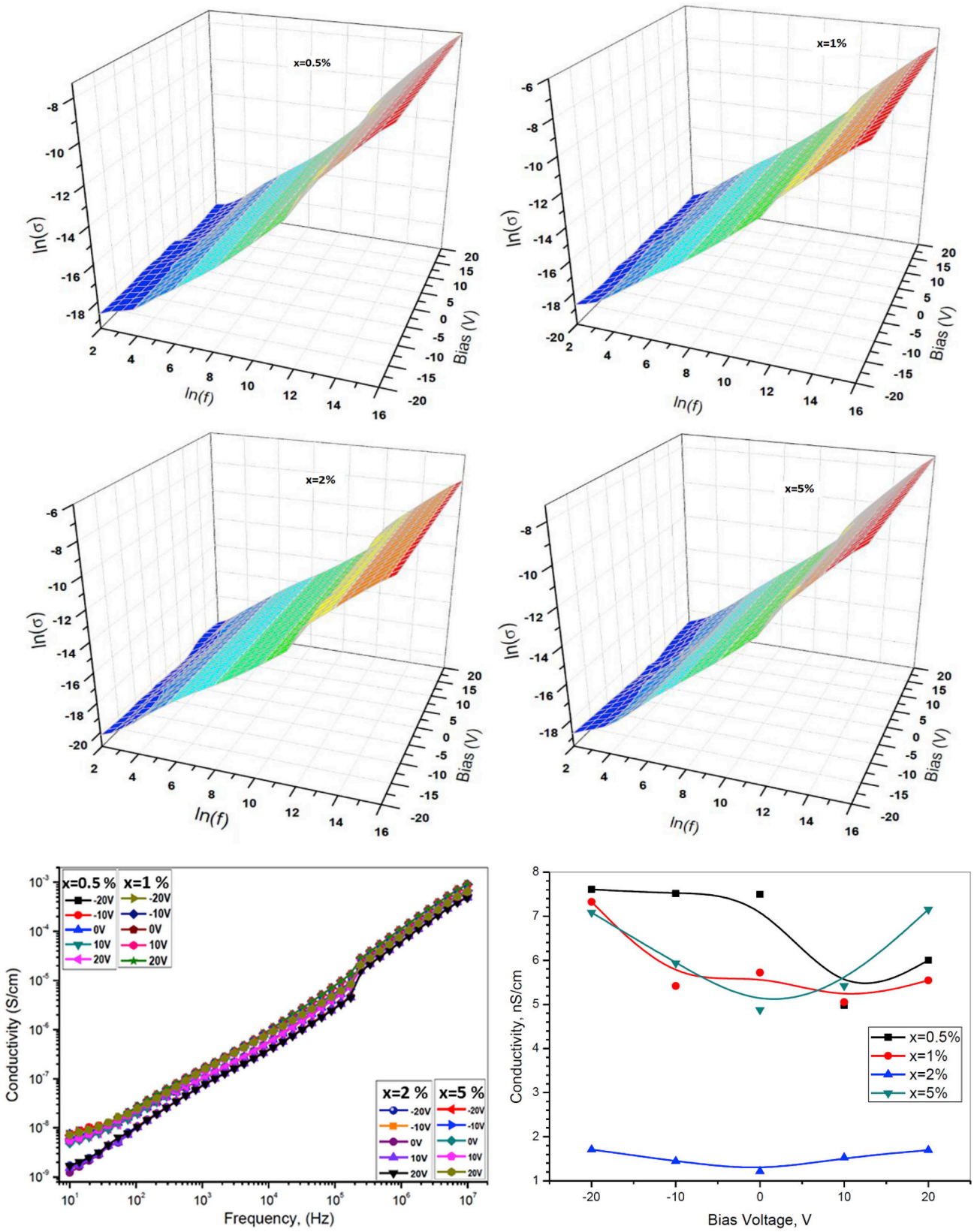

Fig. 7. 3D and 2D characteristic plots of conductivity for BT-ST/$(SiO_2)_x$ nanocomposites as functions of frequency up to 10 MHz, and dc bias ranging between −20 V and 20 V at room temperature.

Last graph in Fig. 7 shows that conductivity varies with both SiO_2%, and *dc* bias at room temperature. It can be noted that conductivity for higher percentages such as x = 2% and 5% has a regular symmetric variation for both positive and negative *dc* bias while the one for the rest fluctuates with applied *dc* bias. This means that absolute *dc* bias causes an increase in conductivity because of the assistance of the

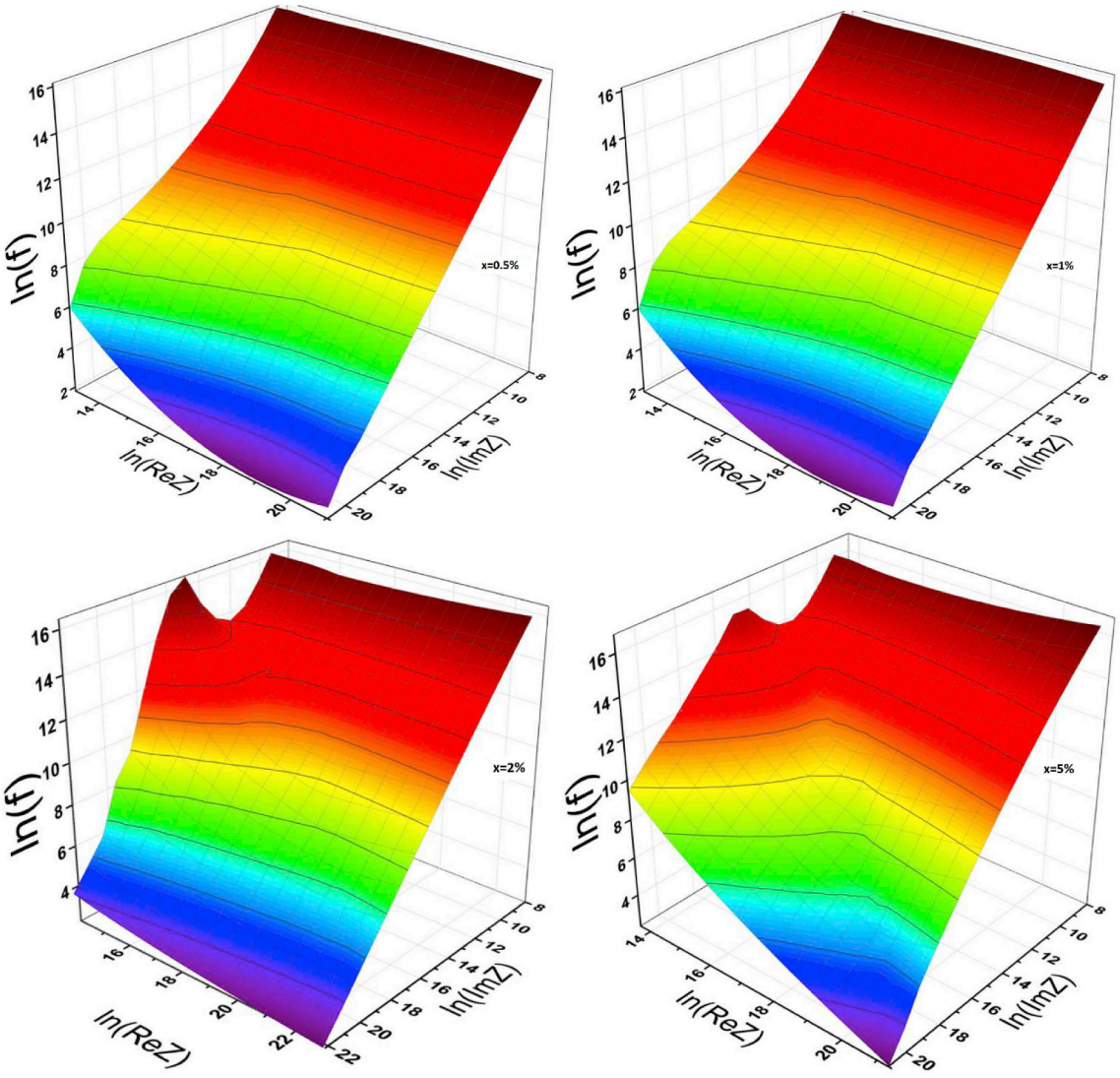

Fig. 8. The resistance-reactance characteristic 3D plots of BT-ST/$(SiO_2)_x$ nanocomposites versus frequency up to 10 MHz.

electric field to conduction mechanism.

3.5.2. Complex impedance and logartmic Nyquist plotting

The dielectric properties for any doped BT-ST ceramics can be typically realized by the volumetric ratio of grains/grain boundaries. At low frequency, the effect of the grain boundaries on conduction mechanism is more dominant than that within grains. Since the grain boundaries are less conductive than grains, the movement of the charge carriers is lowered due to poorer electrical conduction at the grain boundaries. BT-ST/$(SiO_2)_x$ nanocomposites are of considerable interest in a similar characteristic pattern because it has been found that grain boundaries are larger than volumetric grains. This usually involves that the grain boundaries in BT-ST/$(SiO_2)_x$ nanocomposites serve as barriers in the mechanism of conduction.

As a characteristic analysis of both micro- and nano-structures, Nyquist plot is a powerful method to explore the effect of BT-ST/$(SiO_2)_x$ nanocomposites on conduction mechanisms. The characteristic 3D Nyquist plots of BT-ST/$(SiO_2)_x$ nanocomposites as frequency up to 10 MHz are shown in Fig. 8 for a variety of SiO_2 percentages at room temperature without any applied dc bias. As can be seen from all the 3D graphs, the Nyquist plots provide some important parameters linked to non-Debye relaxation behavior. Figs. 7 and 8 show that the resistance (ReZ) depends weakly on frequency while reactance (ImZ) leads to a strong dependency. So, ImZ decreases with an elavated frequency as ReZ shows a small effect because of the dominant reactive influence on conduction mechanism. 3D Nyquist plots of ln(ReZ)-ln(ImZ)-ln(f) of BT-ST/$(SiO_2)_x$ nanocomposites shows that ImZ obey somehow power law dependence on frequency ($\alpha\omega^{-n}$) for a variety of SiO_2 percentages. However, ReZ illustrates opposite tendencies, but irregular and less effective against lower frequency with some degree of SiO_2 content dependencies. At higher frequencies, both ReZ and ImZ showed some decrease tendencies in the frequency-dependency related to the exponent power law. This can be attributable to the volumetric ratio of grain/grain boundries as mention earlier. In most cases, BT-ST NPs may comprise of some heterogeneous granular structures. Thus, some kind of semicircular arc caused by a variety of electrically active regions can originate from grains, grain boundaries, and electrode polarization effects. The semicircular arc can be relevant to formation of grains at higher frequencies. There would be some acceptable explanations based on the appearance of a relevant arc induced by the effect of grains and grain boundaries [48]. The other important tendencies could be based on SiO_2 levels and type within BT-ST NPs. It can be clearly seen that ReZ is lower for grains but higher for grain boundaries. So, it is supposed that tendencies of conductivity at lower frequency are attributable to the charge polarization on grain boundaries.

3.5.3. Dielectric properties

3.5.3.1. Dielectric constant. The dielectric constant of BT-ST/$(SiO_2)_x$ nanocomposites is shown in both the 3D and 2D plots of Fig. 9 versus

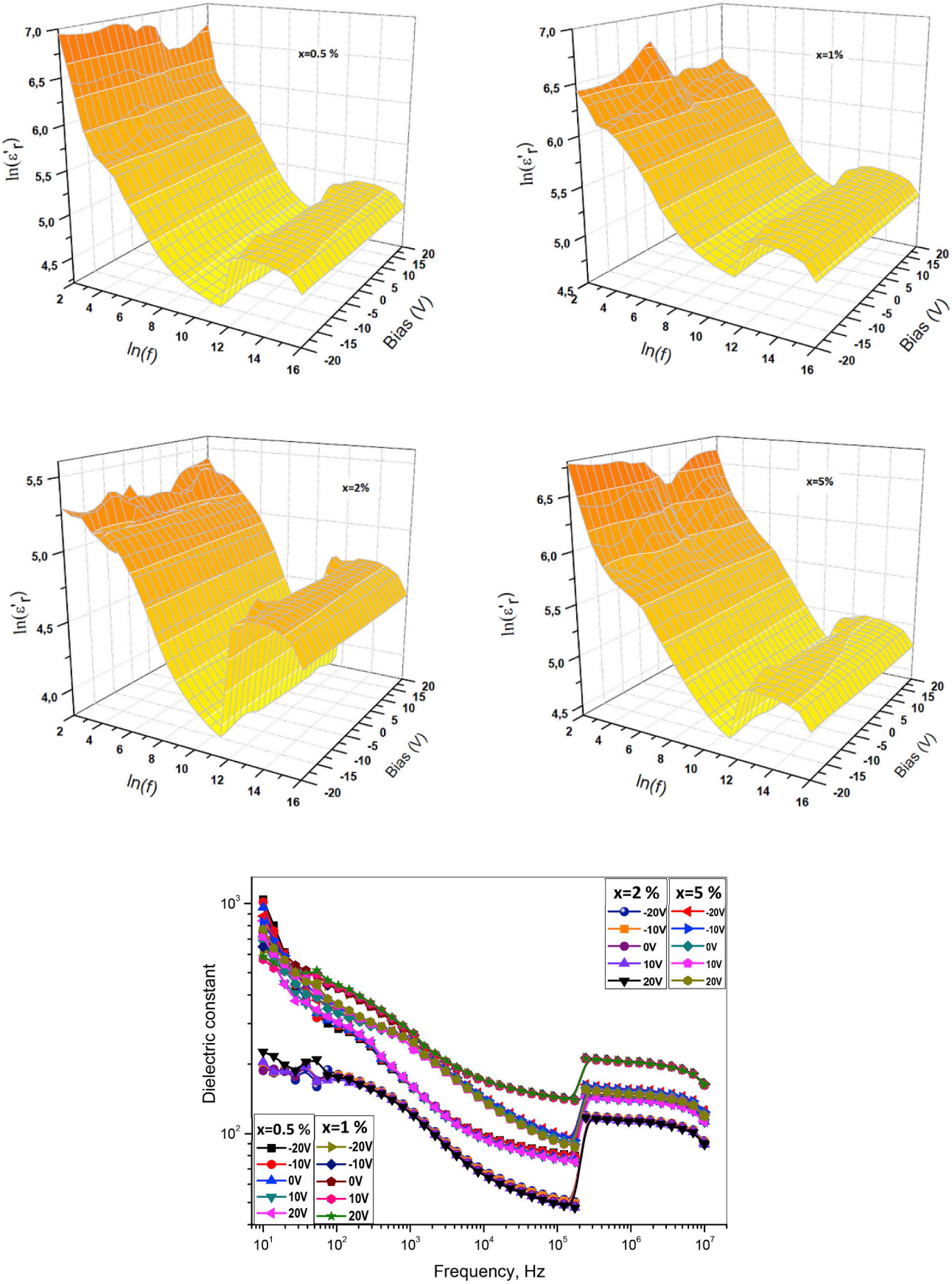

Fig. 9. 3D and 2D characteristic plots of dielectric constant of BT-ST/$(SiO_2)_x$ nanocomposites as functions of frequency up to 10 MHz, and dc bias ranging between −20 V and 20 V at room temperature.

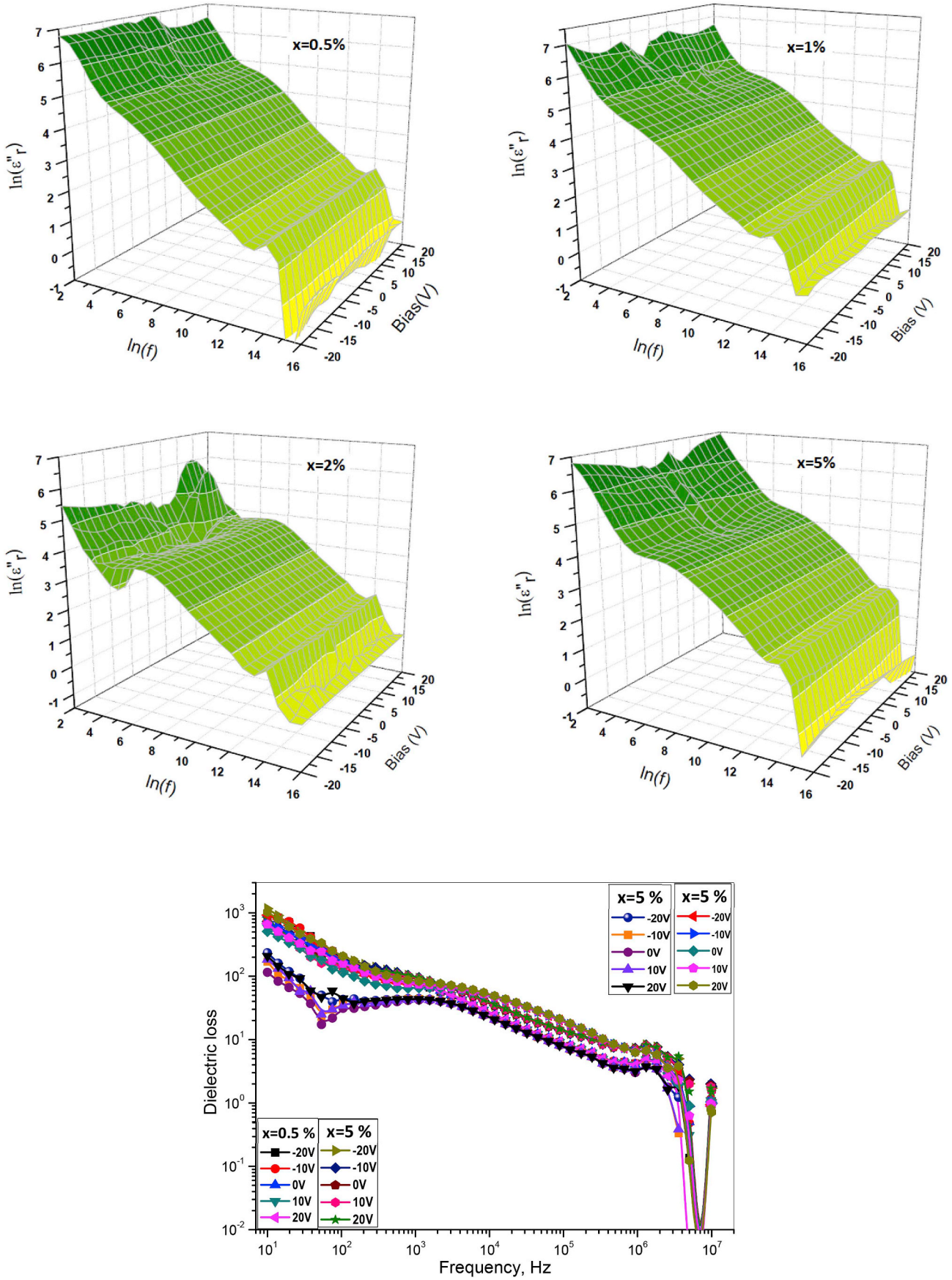

Fig. 10. 3D and 2D characteristic plots of dielectric loss of BT-ST/$(SiO_2)_x$ nanocomposites as functions of frequency up to 10 MHz, and dc bias ranging between − 20 V and 20 V at room temperature.

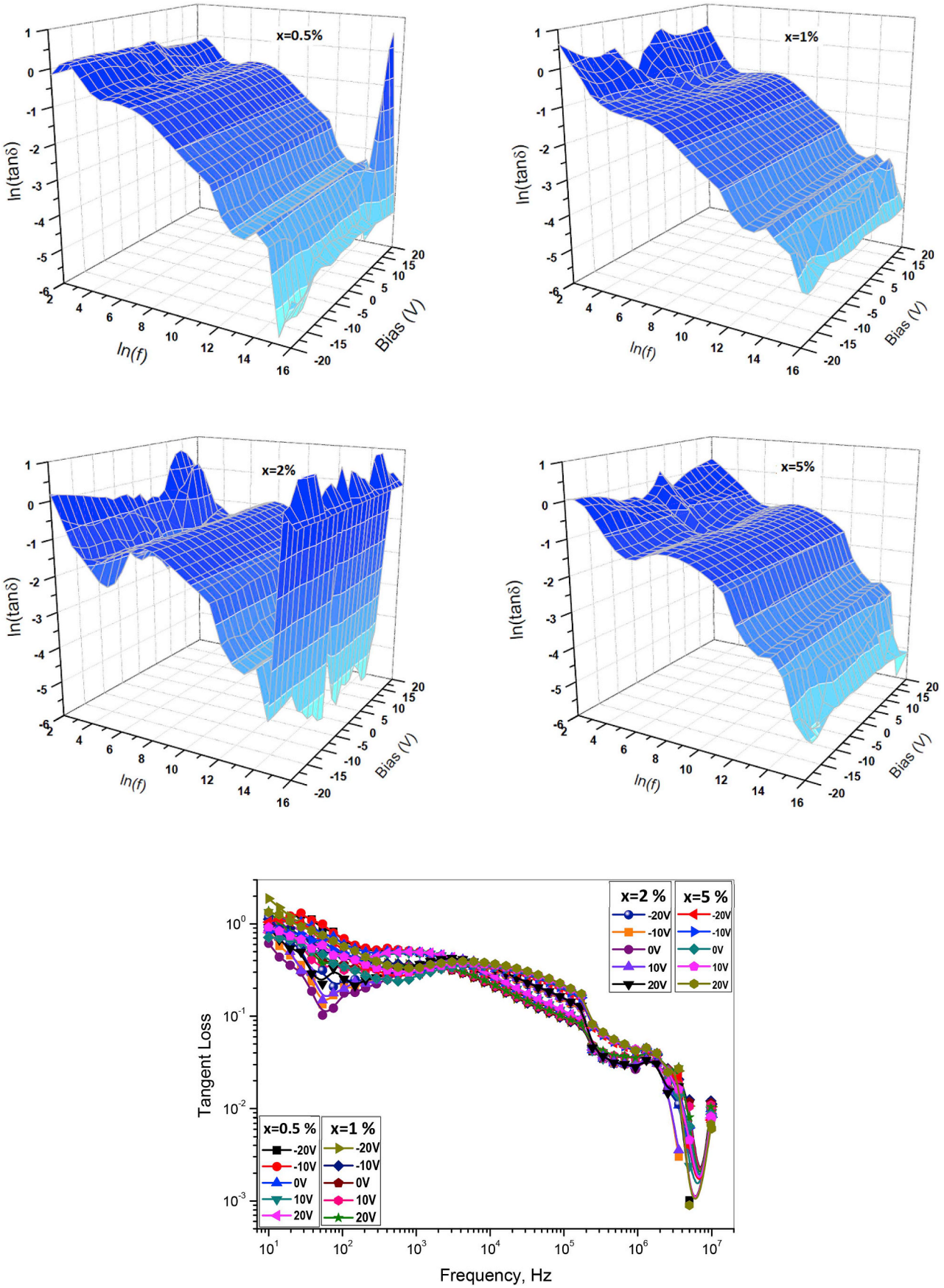

Fig. 11. 3D and 2D characteristic plots of dielectric tangent loss of BT-ST/$(SiO_2)_x$ nanocomposites as functions of frequency up to 10 MHz, and dc bias ranging between −20 V and 20 V at room temperature.

frequency up to 10 MHz and *dc* bias varying from −20 V to 20 V at room temperature for various SiO_2 content. It is evident to note that *dc* bias set develops a similar tendency for each content of SiO_2 with a slight fluctuation. So, the dielectric constant increases with a sequential order such as x = 2%, 0.5%, 5% and 1% at medium frequencies as it shows an almost steady reduction in the entire frequency range, except for some fluctuations, with a sudden boost at about 200 kHz. It is also observed that SiO_2 percentages provide a highly influential contribution with dielectric constant resulting in a considerable range of variations between 198.8 and 1040.3 at lowest frequency of 10 Hz. Former values decrease with a kind of power law tendencies down to 50 and 180 at a frequency of 200 kHz, respectively, and then it increases sharply over a value 100, finally, all of them as a set decline softly with a power law at a frequency up to 10 MHz. Furthermore, a slight change of dielectric constant with *dc* biases between *-20V* and *20V* can also be noticed except for some slight fluctuations. It is also emphasized that the lowest SiO_2 content of x = 0.5% gives us the highest dielectric constant of about 1040 while the BT-ST/$(SiO_2)_2$ nanocomposite leads us a value of about 200 (five times lower) [46]. It should be noticed that power law exponent is strongly dependent on a certain SiO_2 content. So, it is a non-linearity dependency on SiO_2 content (Fig. 9). In addition to all above explanations, one of our purpose of the investigation for BT-ST/$(SiO_2)_x$ nanocomposites is for surveying the possibility to develop its high dielectric constant by a kind of modifications of SiO_2 content level in BT-ST. It is obvious to comprehend how to overwhelm the formation of grain-grain boundaries, and how to inhibit the propagation of Ti species is an important challenge for the realization of an alternative "*high-k gate dielectric*" applications [49]. In general, the functionality of dielectric constant with frequencies confirmed that the SiO_2 content had a prominent influence on the dielectric properties.

3.5.3.2. Dielectric loss. The dielectric loss ε_r'' is an important parameter to evaluate the dissipation of energy through the motion of charge carriers in an ac electric field stimulus with a polarization alteration. Hence, both 2D and 3D representations of ε_r'' of BT-ST/$(SiO_2)_x$ nanocomposites versus function of frequencies are illustrated in Fig. 10 for various SiO_2 content at room temperature. It is obvious to realize from the *log-log* plots in Fig. 10 that dielectric loss corresponds to a power law dependency having a certain exponent value, n;

$$\varepsilon_r''(\omega, x) = \varepsilon_r''(T, x)\omega^{-n}$$

The curve for the bundle cluster associated with x = 2% nanocomposite shows a very different trend at frequencies below 1.0 kHz. So, a sharp drop is observed at frequencies over 2.0 MHz for all the curves. The dielectric loss for the remaining set follows the power law specified in the above formulation. At higher frequencies, very low $\varepsilon_r^?$ and relatively high ε_r' present a leading benefit for BT-ST NPs [49]. The reason of the fluctuation in $\varepsilon_r^?$ values at high SiO_2 amount, especially for x = 2% can be attributed to their incorporated grain-grain boundaries. It is obvious that the ε_r' shows less variation for same SiO_2 content level compared to the $\varepsilon_r^?$ [47].

3.5.3.3. Dissipation factors. The dielectric tangent loss, $tan\delta$, of BT-ST/$(SiO_2)_x$ nanocomposites versus function of frequencies is demonstrated in Fig. 11 for a variety of SiO_2 content at room temperature. It is obvious to realize from both 2D and 3D *log-log* plots that tangent loss as a dissipation factor complies slightly with a power law with a certain exponent in some similarities to the dielectric loss curvatures. However, it contains more fluctuation along the elevated frequency regions as well as *dc* bias values varying from −20 V up to 20 V. At higher frequencies over 2.0 MHz, it represents a sharp decline for all the curves in the graph, and then increases again for just SiO_2 content of x = 2%, but also is observed to increase partially for that of x = 0.5%.

4. Conclusion

In this study, $BaTiO_3$–$SrTiO_3$/$(SiO_2)_x$ nanocomposites (x = 0, 0.5, 1, 2 and 5%) were produced through solid state reaction. According to XRD analysis, two distinct phases of $BaTiO_3$ and $SrTiO_3$ with cubic structure were detected. No such impurity was noticed for x ≤ 0.5% nanocomposite. However, $Ba_2TiSi_2O_8$ secondary phase starts to appear for x ≥ 1%. No impurity was observed when SiO_2 content is lower than x = 0.5%, however, with further increasing SiO_2 content to x ≥ 1%, $Ba_2TiSi_2O_8$ secondary phase were detected. A change in optical band gap energy was observed with SiO_2 inclusions in BT-ST, which could be attributed to grains size variations, presence of impurities and synergetic effects, etc. The detailed investigation of the conductivity, the dielectric constant and loss in the measured frequencies of 10 Hz to 10 MHz, and externally applied dc biases ranging from −20 V to 20 V as well as low tangent loss is observed to be very important for the application of the BT-ST/$(SiO_2)_x$ nanocomposites in many types of electronic devices. Most of the parameters mentioned above obey exponent power law against frequencies with various exponent values. Electrical conduction mechanism shows that ac conductivity depends linearly on frequencies in the log-log graphs, but almost independent of externally applied *dc* bias. The dielectric constant and dielectric loss and dissipation factor are found to reduce with the elevated frequency almost obeying a power law exponent.

Acknowledgments

This study was supported by the Institute for Research & Medical Consultations (Projects application No. 2017-IRMC-S-3, No. 2018-IRMC-S-2 and No. 2017-576-IRMC) of Imam Abdulrahman Bin Faisal University (IAU – Saudi Arabia).

References

[1] C.D. Chandler, C. Roger, M.J. Hampden-Smith, Chemical aspects of solution routes to perovskite-phase mixed-metal, Chem. Rev. 93 (1993) 1205–1241.
[2] M.A. Pena, J.L.G. Fierro, Chemical structures and performance of perovskite oxides, Chem. Rev. 101 (2001) 1981–2017.
[3] S. Royer, D. Duprez, F. Can, X. Courtois, C. Batiot-Dupeyrat, S. Laassiri, H. Alamdari, Perovskites as substitutes of noble metals for heterogeneous catalysis: dream or reality, Chem. Rev. 114 (2014) 10292–10368.
[4] W. Maison, R. Kleeberg, R.B. Heimann, S. Phanichphant, Phase content, tetragonality, and crystallite size of nanoscaled barium titanate synthesized by the catecholate process: effect of calcination temperature, J. Eur. Ceram. Soc. 23 (2003) 127–132.
[5] M.Z.-C. Hu, G.A. Miller, E.A. Payzant, C.J. Rawn, Homogeneous (Co)precipitation of inorganic salts for synthesis of monodispersed barium titanate particles, J. Mater. Sci. 35 (2000) 2927–2936.
[6] J.R.G. Franco, Ferroelectric Crystals vol. 402, Dover Publications Inc., New York, 1993.
[7] Y. Mao, S. Banerjeea, S.S. Wong, Hydrothermal synthesis of perovskite nanotubes, Chem. Commun. (2003) 408–409.
[8] Q. Kuang, S. Yang, Template synthesis of single-crystal-like porous $SrTiO_3$ nanocube assemblies and their enhanced photocatalytic hydrogen evolution, ACS Appl. Mater. Interfaces 5 (2013) 3683–3690.
[9] Z. Wang, S. Jiang, G. Li, M. Xi, T. Li, Synthesis and characterization of $Ba_{1-x}Sr_xTiO_3$ nanopowders by citric acid gel method, Ceram. Int. 33 (2007) 1105.
[10] U. Ellerkmann, R. Liedtke, U. Boettger, R. Waser, Interface-related thickness dependence of the tunability in $BaSrTiO_3$ thin films, Appl. Phys. Lett. 85 (2004) 4708.
[11] C. Mao, X. Dong, T. Zeng, H. Chen, F. Cao, Nonhydrolytic sol–gel synthesis and dielectric properties of ultrafine-grained and homogenized $Ba_{0.70}Sr_{0.30}TiO_3$, Ceram. Int. 34 (2008) 45.
[12] L. Wang, H. Kang, D. Xue, Ch Liu, Synthesis and characterization of $Ba_{0.5}Sr_{0.5}TiO_3$ nanoparticles, J. Cryst. Growth 311 (2009) 605–607.
[13] S. Sreekantan, A.F.M. Noor, Z.A. Ahmad, R. Othman, A. West, D. Sinclair, Characterization of $Ba_{0.9}Sr_{0.1}TiO_3$ prepared by low temperature chloride aqueous synthesis, J. Mater. Sci. 42 (2007) 2492.
[14] B.R. Priya Rani, M.T. Sebastian, The effect of glass addition on the dielectric properties of barium strontium titanate, J. Mater. Sci. Mater. Electron. 19 (2008) 39.
[15] Z. Wang, S. Jiang, G. Li, M. Xi, T. Li, Synthesis and characterization of $Ba_{1-x}Sr_xTiO_3$ nanopowders by citric acid gel method, Ceram. Int. 33 (2007) 1105.
[16] K.A. Razak, A. Asadov, J. Yoo, E. Haemmerle, W. Gao, Structural and dielectric properties of barium strontium titanate produced by high temperature hydrothermal method, J. Alloy. Comp. 449 (2008) 19.

[17] Y.B. Khollam, S.V. Bhoraskar, S.B. Deshpande, H.S. Potdar, N.R. Pavaskar, S.R. Sainkar, S.K. Date, Simple chemical route for the quantitative precipitation of barium–strontium titanyl oxalate precursor leading to $Ba_{1-x}Sr_xTiO_3$ powders, Mater. Lett. 57 (2003) 1871.
[18] P. Dulian, W. Bąk, K. Wieczoek-Ciurowa, C. Kajtoch, Dielectric behaviour of $BaTiO_3$-$SrTiO_3$ solid solutions fabricated by high-energy ball milling, Key Eng. Mater. 605 (2014) 63–66.
[19] C. Liu, P. Liu, X. Lu, C. Gao, G. Zhu, X. Chen, A simple method to synthesize $Ba_{0.6}Sr_{0.4}TiO_3$ nano-powders through high-energy ball-milling, Powder Technol. 212 (2011) 299.
[20] Zhengwei Xiong, Weiguo Sun, Xuemin Wang, Fan Jiang, Weidong Wu, Dielectric enhancement of $BaTiO_3/SrTiO_3$ superlattices with embedded Ni nanocrystals, J. Alloy. Comp. 513 (2012) 300–303.
[21] Chengyue Tian, Feifei Wang, Ye Xiang, Yiqun Xie, Tao Wang, Yanxue Tang, Dazhi Sun, Wangzhou Shi, Bipolar fatigue-resistant behavior in ternary $Bi_{0.5}Na_{0.5}TiO_3$–$BaTiO_3$–$SrTiO_3$ solid solutions, Scripta Mater. 83 (2014) 25–28.
[22] Byoung-Ki Lee, Yang-Il Jung, Suk-Joong L. Kang, Janusz Nowotny, {111} twin formation and abnormal grain growth in barium strontium titanate, J. Am. Ceram. Soc. 86 (2003) 155–160.
[23] K.B. Chong, Improvement of dielectric loss tangent of Al_2O_3 doped $Ba_{0.5}Sr_{0.5}TiO_3$ thin films for tunable microwave devices, J. Appl. Phys. 95 (2004) 1416.
[24] J. Wang, L. Tang, B. Shen, J.i Zhai, Property optimization of BST based composite glass ceramics for energy-storage applications, Ceram. Int. 40 (2014) 2261–2266.
[25] W. Stöber, A. Fink, E. Bohn, Controlled growth of mono disperse silica spheres in the micron size range, J. Colloid Interface Sci. 26 (1968) 62–69.
[26] Yanjie Luo, Yongping Pu, Panpan Zhang, Jiaojiao Zhao, Yurong Wu, Yuwen Liu, Study on dielectric properties of SiO_2-doped $BaTiO_3$ ceramics, Ferroelectrics 492 (2016) 10–16.
[27] E.P. Gorzkowski, M.J. Pan, B. Bender, C.C.M. Wu, Glass-ceramics of barium strontium titanate for high energy density capacitors, J. Electroceram. 18 (2007) 269–276.
[28] J.S. Park, Y.H. Han, Nano size $BaTiO_3$ powder coated with silica, Ceram. Int. 31 (2005) 777–782.
[29] M. Cernea, B.S. Vasile, A. Boni, A. Iuga, Synthesis, structure characterization and dielectric properties of Nb doped $BaTiO_3/SiO_2$ core-shell heterostructure, J. Alloy. Comp. 587 (2014) 553–559.
[30] Y. Zhang, M. Cao, Z. Yao, Z. Wang, Z. Song, A. Ullah, H. Hao, H. Liu, Effects of silica coating on the microstructures and energy storage properties of $BaTiO_3$ ceramics, Mater. Res. Bull. 67 (2015) 70–76.
[31] A.J. Shuskus, D.J. Quinn, D.E. Cullen, Charge storage characteristics of MIS structures employing dual-insulator composites of HfO_2–SiO_2 and $SrTiO_3$–SiO_2, Appl. Phys. Lett. 23 (1973) 184.
[32] Chun-Chieh Lin, Li-Wen Lai, Chih-Yang Lin, Tseung-Yuen Tseng, $SrTiO_3$–SiO_2 oxide films for possible high-k gate dielectric applications, Thin Solid Films 515 (2007) 8005–8008.
[33] Zheng Wang, Shenglin Jiang, Guangxing Li, Mingpeng Xi, Tao Li, Synthesis and characterization of $Ba_{1-x}Sr_xTiO_3$ nanopowders by citric acid gel method, Ceram. Int. 33 (2007) 1105–1109.
[34] Naghi Shaban, Mahmood Bahar, Synthesis and characterization of Fe and Ni Co-doped $Ba_{0.6}Sr_{0.4}TiO_3$ prepared by sol-gel technique, J. Theor. Comput. Sci. 4 (2017) 157.
[35] Qingwei Du, Wei Zhang, Hao Ma, Zheng Jia, Bo Zhou, Yiqun Li, Immobilized palladium on surface-modified Fe_3O_4/SiO_2 nanoparticles: as a magnetically separable and stable recyclable high-performance catalyst for Suzuki and Heck cross-coupling reactions, Tetrahedron 68 (2012) 3577–3584.
[36] Yi-Hsin Lien, Tzong-Ming Wu, Preparation and characterization of thermosensitive polymers grafted onto silica-coated iron oxide nanoparticles, J. Colloid Interface Sci. 326 (2008) 517–521.
[37] Y. Slimani, H. Gunguneş, M. Nawaz, A. Manikandan, H.S. El Sayed, M.A. Almessiere, H. Sözeri, S.E. Shirsath, I. Ercan, A. Baykal, Magneto-optical and microstructural properties of spinel cubic copper ferrites with Li-Al co substitution, Ceram. Int. 44 (2018) 14242–14250.
[38] X. Li, Y. Hou, Q. Zhao, L. Wang, A general, one-step and template-free synthesis of sphere-like zinc ferrite nanostructures with enhanced photocatalytic activity for dye degradation, J. Colloid Interface Sci. 358 (2011) 102.
[39] A.S. Ahmed, S.M. Muhamed, M.L. Singk, S. Tabassum, A.H. Naqvi, A. Azam, Band gap narrowing and fluorescent properties of nickel doped SnO_2 nanoparticles, J. Lumin. 131 (2011) 1–6.
[40] R.B. Kale, C.D. Lokhande, Influence of air annealing on the structural, optical and electrical properties of chemically deposited CdSe nano-crystallites, Appl. Surf. Sci. 223 (2004) 343–351.
[41] J.T.S. Irvine, D.C. Sinclair, A.R. West, Electroceramics: characterization by impedance spectroscopy, Adv. Mater. 2 (1990) 132.
[42] M.A. Almessiere, B. Unal, A. Baykal, I. Ercan, Electrical properties of cerium and yttrium Co-substituted strontium nanohexaferrites, J. Inorg. Organomet. Polym. (2018), https://doi.org/10.1007/s10904-018-1010-9.
[43] B. Unal, İ.S. Ünver, H. Güngüneş, U. Topal, A. Baykal, H. Sözeri, Microwave, dielectric and magnetic properties of Mg-Ti substituted NiZn-ferrite nanoparticles, Ceram. Int. 42 (2016) 17317–17331.
[44] B. Unal, Z. Durmus, H. Kavas, A. Baykal, M.S. Toprak, Synthesis, conductivity and dielectric characterization of salicylic acid- Fe_3O_4 nanocomposite, Mater. Chem. Phys. 123 (2010) 184.
[45] B. Ünal, A. Baykal, Effect of Zn substitution on electrical properties of nanocrystalline cobalt ferrite, J. Supercond. Nov. Magnetism 27 (2014) 469.
[46] B. Bajac, J. Vukmirovic, D. Tripkovic, E. Djurdjic, J. Stanojev, Ž. Cvejic, B. Škoric, V.V. Srdic, Structural characterization and dielectric properties of $BaTiO_3$ thin films obtained by spin coating, Process. Appl. Ceram. 8 (2014) 219–224.
[47] Yanjie Luo, Yongping Pu, Panpan Zhang, Jiaojiao Zhao, Yurong Wu, Yuwen Liu, Study on dielectric properties of SiO_2-doped $BaTiO_3$ ceramics, Ferroelectrics 492 (1) (2016) 10–16.
[48] Shihua Ding, Tianxiu Song, Xiaojing Yang, Guanghua Luo, Effect of grain size of $BaTiO_3$ ceramics on dielectric properties, Ferroelectrics 402 (1) (2010) 55–59.
[49] C.-C. Lin, L.-W. Lai, C.-Y. Lin, T.-Y. Tseng, SrTiO3–SiO2 oxide films for possible high-k gate dielectric applications, Thin Solid Films 515 (2007) 8005–8008.